LOW-VELOCITY COLLISIONS OF CENTIMETER-SIZED DUST AGGREGATES

E. BEITZ[1], C. GÜTTLER[1], J. BLUM[1], T. MEISNER[2], J. TEISER[2], AND G. WURM[2]

[1] Institut für Geophysik und extraterrestrische Physik, Technische Universität zu Braunschweig, Braunschweig, Germany; e.beitz@tu-braunschweig.de
[2] Universität Duisburg-Essen, Fakultät für Physik, Lotharstr. 1, 47048 Duisburg, Germany

ABSTRACT

Collisions between centimeter- and decimeter-sized dusty bodies are important in understanding the mechanisms leading to the formation of planetesimals. We performed laboratory experiments to study the collisional behavior of dust aggregates in this size range at velocities below and around the fragmentation threshold. We developed two independent experimental setups with the same goal: to study the effects of bouncing, fragmentation, and mass transfer in free particle–particle collisions. The first setup is an evacuated drop tower with a free-fall height of 1.5 m, providing us with 0.56 s of microgravity time, so that we observed collisions with velocities between 8 mm s^{-1} and 2 m s^{-1}. The second setup is designed to study the effect of partial fragmentation (when only one of the two aggregates is destroyed) and mass transfer in more detail. It allows for the measurement of the accretion efficiency because the samples are safely recovered after the encounter. At very low velocities, we found that bouncing was as expected, while the fragmentation velocity of 20 cm s^{-1} was significantly lower than expected. We present the critical energy for disruptive collisions $Q^\star$, which were at least two orders of magnitude lower than previous experiments in the literature. In the wide range between bouncing and disruptive collisions, only one of the samples fragmented in the encounter, while the other gained mass. The accretion efficiency on the order of a few percentage points of the particle's mass depends on the impact velocity and the sample porosity. Our results will have consequences for dust evolution models in protoplanetary disks as well as for the strength of large, porous planetesimal bodies.

Key words: accretion, accretion disks – methods: laboratory – planets and satellites: formation – protoplanetary disks

Online-only material: animations, color figures

1. INTRODUCTION

In a protoplanetary disk (PPD), many collisions between dust aggregates take place. The relative velocities between these particles, caused by Brownian motion, differential drift motions, and gas turbulence, depend on their sizes (see, e.g., Weidenschilling & Cuzzi 1993; Weidling et al. 2009). According to the simulations of Zsom et al. (2010), the largest particles growing in a minimum mass solar nebula (MMSN) model are about 2 cm in diameter. For particles of this size, collision velocities of about 10 cm s^{-1} are expected. However, different PPD models predict a wide range of collision velocities for centimeter-sized dust aggregates, ranging from about 1 cm s^{-1} in the model of Desch (2007) to about 5 m s^{-1} in the low-density model of Andrews & Williams (2007). Thus, it is interesting to experimentally investigate the collision behavior of centimeter-sized dust aggregates in a wide range of velocities, and to assess the validity of the dust collision model by Güttler et al. (2010) and the dust evolution model by Zsom et al. (2010). For low-velocity collisions between centimeter-sized dust aggregates, it is indispensable to design an experimental setup in which the collisions take place without the overwhelming influence of gravity. In Section 2, we describe two experimental setups with which we can investigate free collisions between two centimeter-sized dust aggregates in a wide velocity range between 8 mm s^{-1} and 2 m s^{-1}. Moreover, the choice of our analog dust particles is explained. Section 3 shows the results of these experiments and Section 4 discusses and interprets these results in terms of their applicability in PPD dust evolution models.

2. EXPERIMENTAL SETUP

To study the effects of dust aggregate collisions for a variety of collision velocities, two slightly different experimental setups

were developed: in the drop-tower setup (Section 2.1), we were able to observe free collisions between centimeter-sized dust aggregates for very low to intermediate impact velocities (0.8–200 cm s^{-1}). In a second setup, in which we studied velocities above the fragmentation threshold (approx. 50 cm s^{-1}, Section 2.2), the samples were—in contrast to the drop-tower setup—not demolished after the encounter, so that a detailed measurement of the mass balance was possible. We used this setup to study the mass transfer between aggregates as a function of the porosity difference and the collision velocity.

2.1. Drop-tower Setup

The first setup is an evacuated drop tower consisting of a glass tube with additional vacuum chambers attached to the top and to the bottom. Outside the glass tube, two cameras are recording the experiment in back-lit illumination (Figure 1).

The main part of the drop tower is the glass tube which has a height of 1.5 m and an inside diameter of 22 cm. Two vacuum chambers are fixed at the top and bottom of the glass tube. Electrical feedthroughs are attached to these chambers to provide the power for a magnetic release mechanism (see below). Additionally, a pressure gauge monitors the vacuum quality, which was 1–10 Pa in all experiments. To perform collisions between two-2-cm diameter dust aggregates, a two-level release mechanism (Figure 2) is attached at the top flange of the upper chamber. The upper level consists of a linear solenoid pushing a nylon string embedded in the sample onto a vertically mounted plate. The lower level comprises a plate with a hole, mounted to a rotary solenoid, where the particle size exceeds the hole diameter and is thus centered in position. By moving the position of the vertical plate, the impact parameter can be
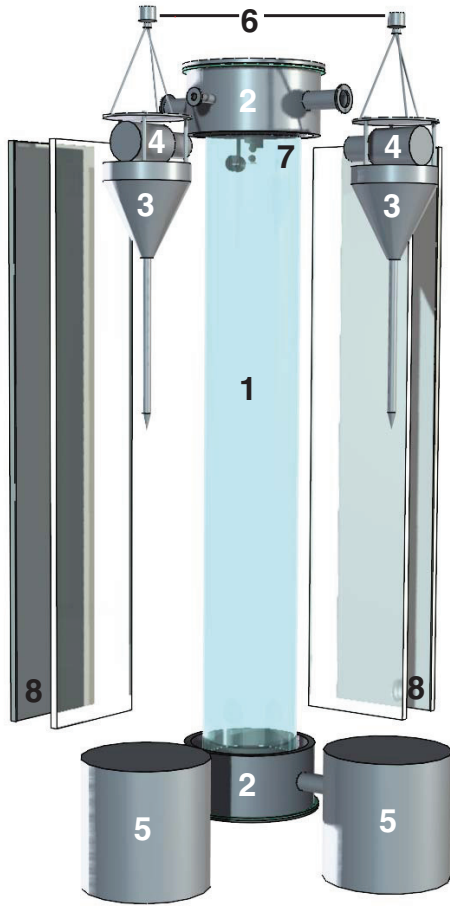
Figure 1. Drop-tower setup consists of (1) a glass tube with a height of 1.5 m and an inside diameter of 22 cm; (2) vacuum chambers with electrical feedthroughs, pressure gauge, and vacuum pump; (3) camera platforms with a streamlined funnel; (4) two high-speed cameras separated by an angle of 90°; (5) buckets filled with sand to decelerate the cameras; (6) electromagnets for attaching the camera platforms to the ceiling; (7) a two-level particle-release mechanism (also see Figure 2); and (8) two LED arrays and diffusion screens for back-lit illumination.

(A color version of this figure is available in the online journal.)

precisely adjusted. The distance between the upper and lower particle edges can be varied between 1 mm and 30 cm.

To be able to record a collision in free fall, two high-speed cameras are dropped outside the glass tube, with their fields of view centered at the center of mass of the free-falling particles. The cameras are each placed on a platform mounted on the top of a streamlined funnel that ends in a steel rod. Due to their shape and weight of about 10 kg, they are trailing the particle (which fall in vacuum) by fewer than 5 mm at the end of their free fall. Prior to the experiment, the camera platforms are fixed on the ceiling with an electromagnet that can be released by switching off the current. The two cameras are separated by an angle of 90°, which provides a three-dimensional observation of the collision. One camera is operated at a picture rate of 261 frames per second, with a field of view of about $6 \times 6 \, \text{cm}^2$ and a resolution of 190 pixels cm^{-1}. The other one is a photo camera, recording with 40 frames per second and a significantly larger field of view ($15 \times 15 \, \text{cm}^2$) at a comparable resolution. A back-lit illumination was created by two LED arrays with diffusion screens at the opposite side of the glass tube.

The experiment is triggered by a microcontroller that controls two time periods: the first one is the relative delay between the
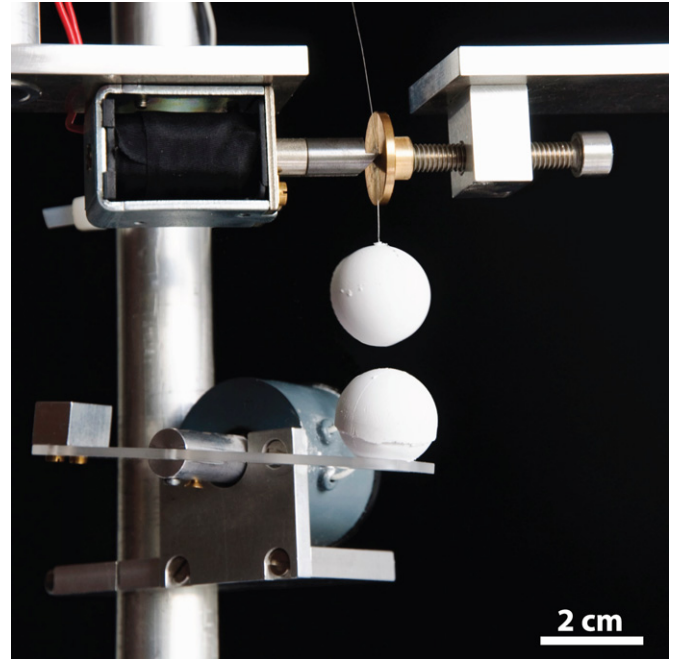

Figure 2. Two-level release mechanism: the upper level consists of a linear solenoid, pressing a nylon string with a metal rod against an adjustable metal plate. The lower level is a plate with a hole mounted on a rotary solenoid.

(A color version of this figure is available in the online journal.)

release of the upper level and the drop of the falling cameras. The second one is the time lag between the cameras and the lower level. The reachable minimal sum of the two time lags is on the order of 1 ms, which leads to the smallest achievable collision velocity of

$$v_{\text{coll}} = g \cdot \Delta t = 9.81 \, \text{m s}^{-2} \cdot 1 \, \text{ms} \approx 1 \, \text{cm s}^{-1}, \qquad (1)$$

where g is the gravitational acceleration. The upper limit of the accomplishable velocities is based on a maximal distance between the edges of the particles of about $\Delta h = 0.3 \, \text{m}$, which yields a collision velocity of $v_{\text{coll}} = \sqrt{2g\Delta h} \approx 2.5 \, \text{m s}^{-1}$.

It is desirable to adjust the collision time to one-half of the free-fall time, so that the same number of images is available for data analysis before and after the collision. To accomplish this, the distance between the particles Δh must be adjusted according to the equation

$$\Delta h = v_{\text{coll}} \left(\frac{t_{\text{freefall}}}{2} - \frac{v}{2g} \right), \qquad (2)$$

with a free-fall time for the 1.5-m drop tower of $t_{\text{freefall}} = 0.55$ s.

The samples used for the particle–particle collisions in this experiment are manufactured in a self-built compression mechanism that consists of a stainless steel mold and an aluminum stamp with a concave shape at one end. The stamp fits into the mold such that a ball of 2 cm diameter can be compressed inside. To avoid dust sticking to the mechanism, the surface is worked with a nanotechnics polish. For half the spheres, a nylon string is embedded on which they were suspended in the upper level of the particle release mechanism (cf. Figure 2).

For each sample, we poured exactly 4.1 g of spherical SiO$_2$ dust (see Section 2.3 for details) into the container and compressed it with the stamp. Because this pressure could not

be perfectly identical in all cases, we expect small variations in the volume-filling factors between $\phi = 0.49$ and $\phi = 0.54$. These values were inferred from the known mass and volume measurement of the falling aggregates for those cases where the spheres were fully visible. Thus, it is not expected that two colliding aggregates are perfectly similar, but rather that one will always be slightly more porous and fragile than the other, which will become important in the discussion. The average difference in the volume-filling factor between two colliding spheres is $\Delta\phi = 0.025 \pm 0.025$.

2.2. Solenoid–Accelerator Setup

In this series of experiments, collisions between dust aggregates with different filling factors at different velocities were studied in a velocity range from 0.5 to 1.4 m s^{-1} and a range in porosity differences from 0.029 to 0.129. Dust aggregates of irregular SiO$_2$ dust (see Section 2.3) were prepared in a similar fashion to the drop-tower experiments (Section 2.1) by compressing dust into a given volume; however, we did not aim to produce spherical particles here but rather compressed cylinders of 30 mm diameter and variable heights. We always used the same mass of (13.02 ± 0.25) g and, by qualitatively varying the compressing pressure, we generated dust aggregates that varied in the filling factor between $\phi = 0.35$ and $\phi = 0.49$. This changes the thickness of the cylindrical aggregate slightly, but the cylindrical dust aggregate typically had a height of about 17 mm. In the drop-tower experiments, the aggregates are destroyed after the collision because they simply crash on the bottom of the experiment chamber. Complementary to this, we aimed here to recover the aggregates after the experiment to allow mass measurement, i.e., to determine the mass balance of the aggregate. To accomplish this, one of the dust aggregates was suspended on a thread that was fixed to an elastic strap. The second aggregate was launched vertically upward and hit the target. The target obtained an upward momentum and was somewhat lifted, while the elastic band decelerated slowly enough on its downward motion to remain intact; any gained mass stayed on the aggregate. With this setup, the particle can behave in the same way as in a free collision and the gained mass can stay intact on the target, so it can be precisely weighted after the encounter. In the first experiments, the more compact aggregate (higher filling factor) survived the collision and gained mass from the less compact aggregate, which fragmented in the collision. Therefore, the compact aggregate was suspended and the less compact aggregate was accelerated. No alteration of the aggregates' conditions could be observed due to the embedded string. As a stable configuration, the compact dust aggregate always had the same filling factor of 0.480 ± 0.006. The setup is sketched in Figure 3. The launcher consists of a solenoid, on which a small platform is mounted. On this platform, the dust aggregate with higher porosity (i.e., the weaker aggregate) is placed. We observed central collisions in which aggregates collided with their mantle face.

The entire assembly was mounted in a vacuum chamber, with an ambient pressure of 0.1 Pa to avoid gas effects during the collision. The collisions at the height of the target were captured in an image sequence with a 2-ms time difference between the frames. Based on these animations, collision velocities were determined, and it was observed that the mass gained in a collision remained on the target during deceleration. The mass of the target was always measured before and after the collisions.
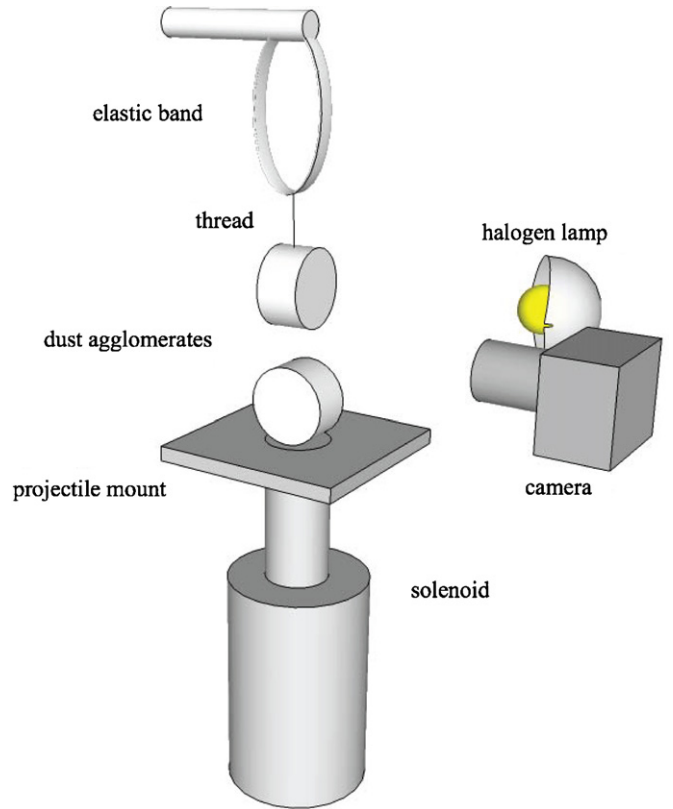

Figure 3. Experimental setup for collisions of the dust cylinders. The solenoid accelerates the lower aggregate, which collides with the upper aggregate, which is suspended on an elastic strip.

(A color version of this figure is available in the online journal.)

2.3. Choice of Analog Material

To prepare samples for an experiment that aims to study the formation of planets, proper analog material has to be chosen. An additional requirement is the commercial availability of the material. We therefore used SiO$_2$ dust of different shapes in the micrometer-size range. This dust has been used in many previous experiments (Blum & Wurm 2008 and references therein), which showed that it can—at least in a mechanical sense—be regarded as representative of the class of silicates. For the drop-tower experiments with spherical aggregates, we used monomers of 1.5 μm diameter (manufacturer: micromod). These grains were well characterized by Heim et al. (1999), and their material properties were analyzed by Blum & Schräpler (2004) and Güttler et al. (2009). For the cylindrical samples in the second setup, we used irregular SiO$_2$ grains in a size range from 0.1 to 10 μm, in which 80% of the mass is in the range between 1 and 5 μm (manufacturer: Sigma-Aldrich). Those irregular grains have also been used in many previous experiments (Blum & Wurm 2008 and references therein). From these experiments, we learned that grain shape plays a minor role in aggregate behavior, and those two species can carefully be regarded as comparable. We will discuss potential differences in Section 4.

3. RESULTS

In this section, we will present the results of our experiments, which include the measurement of coefficients of restitution, strength of fragmentation, and mass transfer. In Section 3.1, we analyze 24 collisions between spherical dust aggregates in a velocity range of 0.8–37 cm s^{-1}, which all led to bouncing.
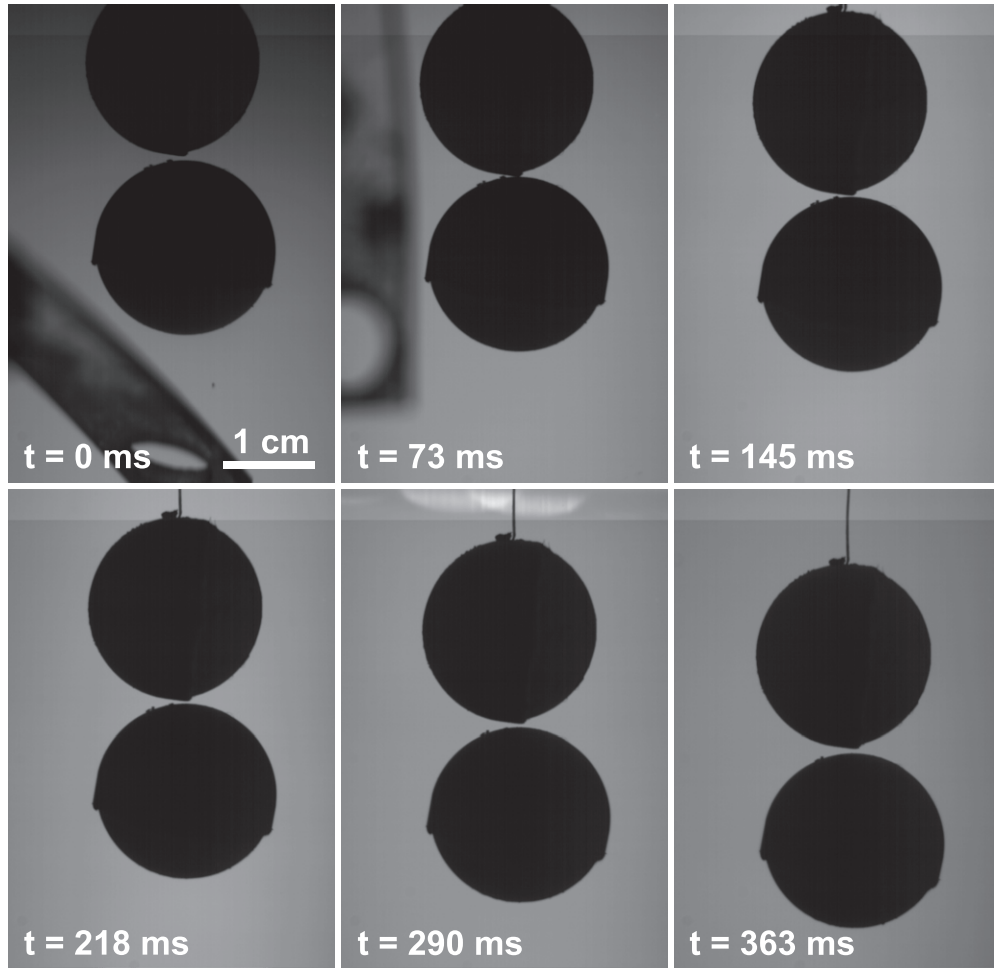
Figure 4. Typical sequence of a bouncing collision at an impact velocity of $v = 8$ mm s^{-1}. The coefficient of restitution for this experiment was $\varepsilon = 0.29$. (An animation of this figure is available in the online journal.)

Table 1
Overview of the Experiments and their Outcomes

Experiment Type	Repetitions	Pressure (Pa)	v_{coll} (cm s^{-1})	ϕ_1	ϕ_2	mass (g)	Collisional Outcome
Drop tower	24	1–10	0.8–37	0.5	0.5	4.1	Bouncing
Drop tower	6	1–10	47–186	0.5	0.5	4.1	Partial fragmentation
Drop tower	5	1–10	24–202	0.5	0.5	4.1	Fragmentation
Solenoid accelerator	20	0.1	50–140	0.39	0.48	13	Fragmentation
Solenoid accelerator	24	0.1	93	0.34–0.45	0.48	13	Fragmentation

For the higher collision velocities, we present 11 collisions of spherical aggregates from 24 to 202 cm s^{-1}, which are described in Section 3.2. In those collisions, one or both aggregates fragmented, and in the cases where only one aggregate fragmented, the preserved aggregate gained mass. Above 190 cm s^{-1}, all collisions led to the disruption of both aggregates. The accretion of one aggregate at the intermediate collision velocity is studied in further detail in Section 3.3. There, we present results from collisions between cylindrical dust aggregates in which we varied not only the collision velocity but also the porosity difference between the aggregates. We performed 24 experiments at a constant collision velocity ($v = 93$ cm s^{-1}) and varied the porosity difference between projectile and target, then 20 experiments with a constant porosity difference ($\Delta\phi = 0.091$) and variable velocities. The particle properties and experimental conditions are shown in Table 1.

3.1. Bouncing Collisions

In a bouncing collision, the two aggregates approach each other, lose energy in the dissipative contact, and depart with a smaller velocity than before the collision. An appropriate parameter to characterize these collisions is the coefficient of restitution:

$$\varepsilon = \frac{v_{\text{after}}}{v_{\text{before}}}. \tag{3}$$

The relation $1 - \varepsilon^2$ is a measure of energy dissipation. Figure 4 shows a typical sequence of a bouncing collision in which the impact velocity was $v = 8$ mm s^{-1}. The second image is close to the moment of contact, and these raw images at a constant time interval already allow a good estimate of the coefficient of restitution (the exact value was calculated as $\varepsilon = 0.29$).
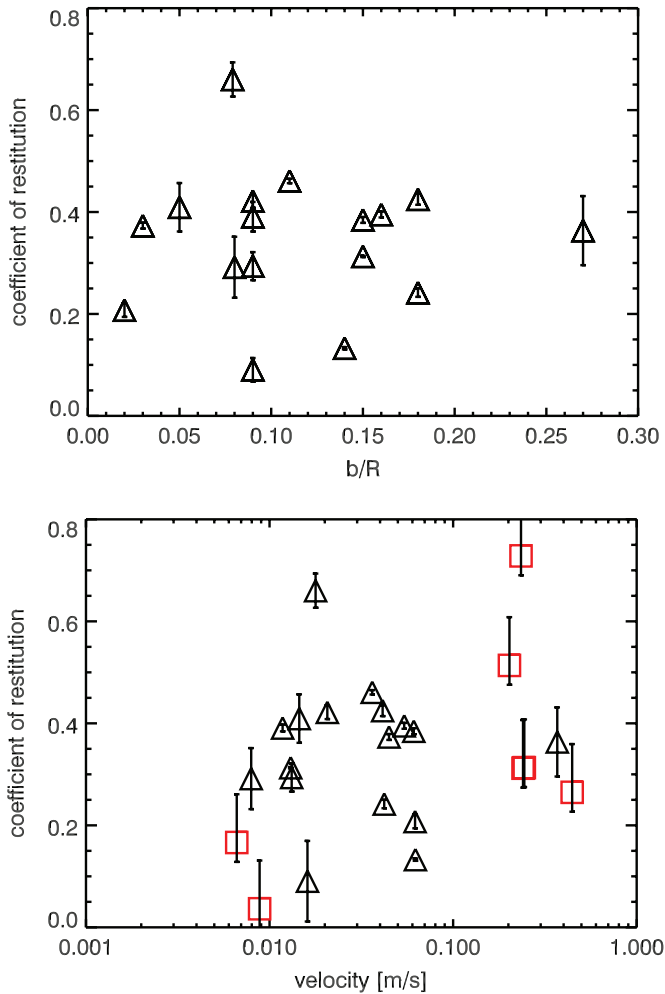
Figure 6. The normalized cumulative number over the coefficient of restitution ε suggests an integrated Gaussian function that yields a normal distribution for ε. The average is at 0.35 ± 0.12. The dashed and dash-dotted lines mark one and two standard deviations, respectively.

Figure 5. The coefficient of restitution ε shows a correlation neither with the impact parameter (top) nor with the impact velocity (bottom). A correlation analysis yields values of -0.003 and 0.1, respectively. Triangles mark all three-dimensional data, and the two-dimensional data are shown (bottom) as squares. (A color version of this figure is available in the online journal.)

The main parameters to measure are the velocities before and after the collision. To achieve this, we binarized the image sequences of both cameras and convolved them with a disk of the proper sphere diameter to compute the temporally resolved, three-dimensional position of the two aggregates. This yielded a precision of 2 pixels, and therefore the quality of the three-dimensional distance between the center of the two particles is shorter than 0.2 mm for a single frame, which becomes even shorter when using a sequence of images. The distance was separately fitted in all three dimensions (for the vertical direction, we chose the fast camera) to get velocity vectors before and after the collision. From these, we can calculate the coefficient of restitution ε, the normalized impact parameter b/R, and the absolute impact velocity v. A rotation of the lower particle was not found in any case. In some cases, the upper particle suspended at the embedded nylon string librated, which led to a rotation of the particle in free fall. To measure the rotation energy and the surface velocity, the positions of two points on the surface relative to the center were followed, and the surface velocity and rotation energy were calculated. That energy was compared with the translational energy, and a threshold was set at 10% to distinguish between rotating and non-rotating impacts. Below, we consider only central collisions with the
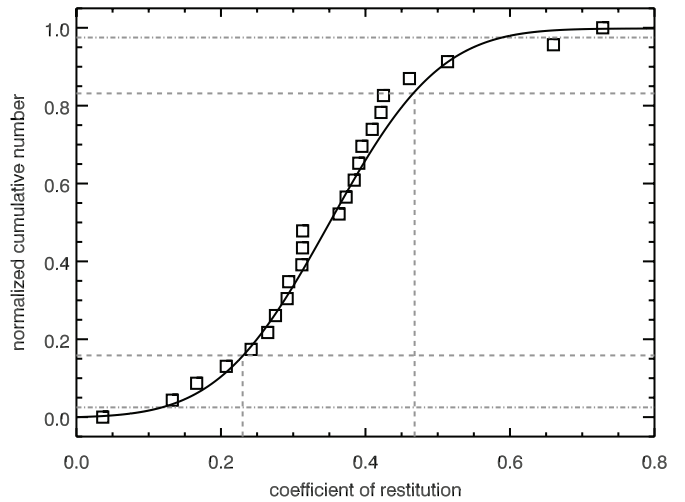
impact parameter $b/R < 0.3$, and experiments with rotating samples are also neglected.

Let us first evaluate the dependence of the coefficient of restitution on the normalized impact parameter b/R. As shown in Figure 5 (top), no strong correlation between these two parameters exists. However, to verify the independence, an analysis of the correlation of these parameters was performed. With this correlation analysis, the parameters b/R and ε were clearly determined to be uncorrelated in the considered parameter range. In Figure 5 (bottom), the coefficient of restitution is plotted over the impact velocity. Here, we increased the number of data points by also including seven collisions in which only the high-speed camera was operating, yielding only two-dimensional information. The collision velocity is dominated by the known vertical component, and the coefficient of restitution was corrected by using the average of the horizontal dimension of the photo camera from the three-dimensional cases. This gave a factor of 0.036, which was added to the coefficient of restitution for these collisions. The error bars are as big as the range of the photo-camera component results in the three-dimensional collisions. For these 24 collisions, Figure 5 (bottom) does not show an obvious correlation between impact velocity and coefficient of restitution; to verify this, we again performed a correlation analysis of these parameters, which yielded a correlation coefficient of 0.1.

Conclusively, all impacts can be regarded as central or near-central collisions, and the coefficient of restitution is correlated neither with the impact parameter nor with the collision velocity in the parameter range considered. We thus plotted the cumulative fraction over the coefficient of restitution (Figure 6). The fit is an integrated Gaussian function,

$$P(\varepsilon) = \int_0^\varepsilon \frac{1}{\sigma_\varepsilon \sqrt{2\pi}} \exp\left(-\frac{(\varepsilon' - \bar{\varepsilon})^2}{2\sigma_\varepsilon^2}\right) d\varepsilon', \qquad (4)$$

with an average coefficient of restitution of $\bar{\varepsilon} = 0.35$ and a standard deviation of $\sigma_\varepsilon = 0.12$. The gray dashed and dash-dotted lines mark one and two standard deviations, respectively.

3.2. Fragmenting Collisions

Increasing the impact velocity led to aggregate fragmentation. In these cases, the coefficient of restitution could not be
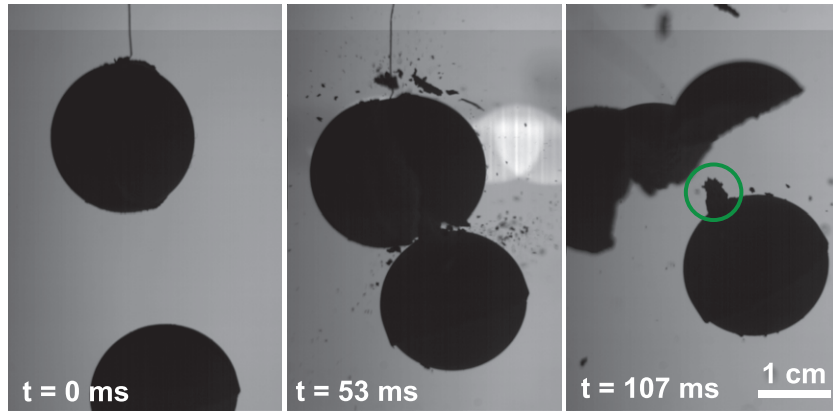
Figure 7. Image sequence of a fragmenting collision at a velocity of 47 cm s^{-1}. The upper aggregate is destroyed, while the lower one gains 0.6% of its original volume.

(An animation and a color version of this figure are available in the online journal.)

calculated, but the strength of fragmentation μ is the characterizing parameter that we determined. It is defined as $\mu_i = M_{f,i}/M_{0,i}$, where $M_{f,i}$ is the largest fragment and $M_{0,i}$ is the total mass of the aggregate i (with $i = 1$ or 2) before fragmentation. The collision velocity was determined in the same way as in Section 3.1, and the size of the largest fragment was measured in one or more representative images from the photo camera. Again, these images were binarized, and the cross-sectional areas of the fragments were fitted with ellipses of the same expanse. The lower estimate for the fragment volume follows from an ellipsoid where the ellipse is rotated around the long axis, and the upper estimate is for rotation around the short axis. Our best estimate is the mean value between those two, and the error follows from the actual values. To calculate the mass of the fragments, we assumed that the volume-filling factor remained unchanged. The results of the fragmentation strength (i.e., the relation $\mu(v)$) are discussed in Section 4.

The slowest impact velocity where fragmentation occurred was at 24 cm s^{-1}, and the fastest bouncing collision was at 37 cm s^{-1}. In Figure 7, a sequence of a collision at 47 cm s^{-1} is presented. This is a typical collision when the velocity is below 187 cm s^{-1}; at these velocities, only one aggregate fragmented, while the other one remained intact and gained mass. This roughly conically shaped dust pile is marked with a green circle in the last image of Figure 7. We assumed this pile to be rotationally symmetric, so we could easily compute its volume: we rotated the image such that the long axis was vertical and measured the width of the pile for each line. Due to the symmetry, each line represented a disk with a height of 1 pixel, and by summing these disks we got the volume. Again, we assumed that the volume-filling factor was unchanged to get the mass of the dust pile. In the example in Figure 7, the intact aggregate has grown by 0.57% of its own mass. The mass gain for all six experiments ranges from 0.05% to 1.1%, and the velocity dependence is presented in Section 3.3. There was no conclusive result regarding whether the upper or lower particle fragmented, because these two possibilities were evenly split between the six experiments. However, when only one particle fragmented, its maximum velocity was about 190 cm s^{-1}. The only exception was one collision at $v = 47$ cm s^{-1} in which both aggregates fragmented. For all collisions above 190 cm s^{-1}, both particles fragmented.

Depending on collision velocity, we qualitatively found the three different collisional outcomes that comprise bouncing,
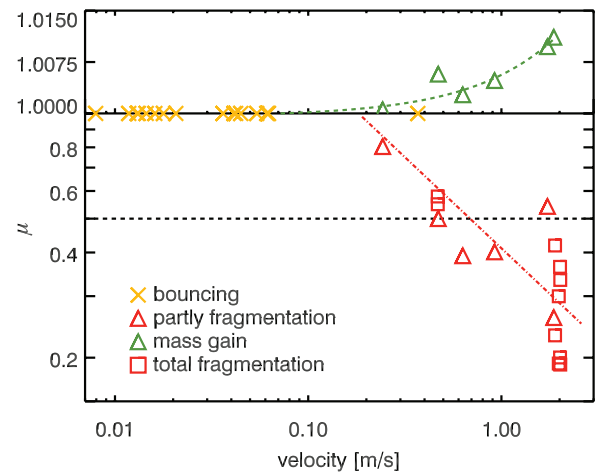

Figure 8. Strength of fragmentation μ over the impact velocity for all drop-tower collisions. The axis for $\mu > 1$ was stretched for better visibility. μ is plotted for each individual sphere to get two data points for each experiment. The values for fragmentation (red) are fitted with a power law (dash-dotted line), and those for mass gain (green) are fitted linearly. The black dashed line at $\mu = 0.5$ denotes the limit for catastrophic fragmentation (cf. Section 4).

(A color version of this figure is available in the online journal.)

fragmentation with mass transfer, and complete fragmentation. In Figure 8, we present a conclusive overview of the outcomes in the drop-tower experiments. The strength of fragmentation for each individual sphere in a collision μ_i is plotted as a function of the collision velocity. In a bouncing collision (previous section), the mass remains constant, so the value for these collisions is unity. Each fragmenting collision yields two μ values, i.e., one for each aggregate. The disruptive collisions are given by the red squares, and those that lead to mass growth yield one negative and one positive μ value (red and green triangles) for the disrupted and grown aggregates, respectively. We adopt a power law for the values with $\mu < 1$, which is given by

$$\mu^-(v) = \left(\frac{v}{(0.18 \pm 0.04)\ \mathrm{m\,s^{-1}}} \right)^{-0.52 \pm 0.09} \qquad (5)$$

and shown as a red dash-dotted line. The vertical axis for the collisions with mass gain is linear and stretched, and we found
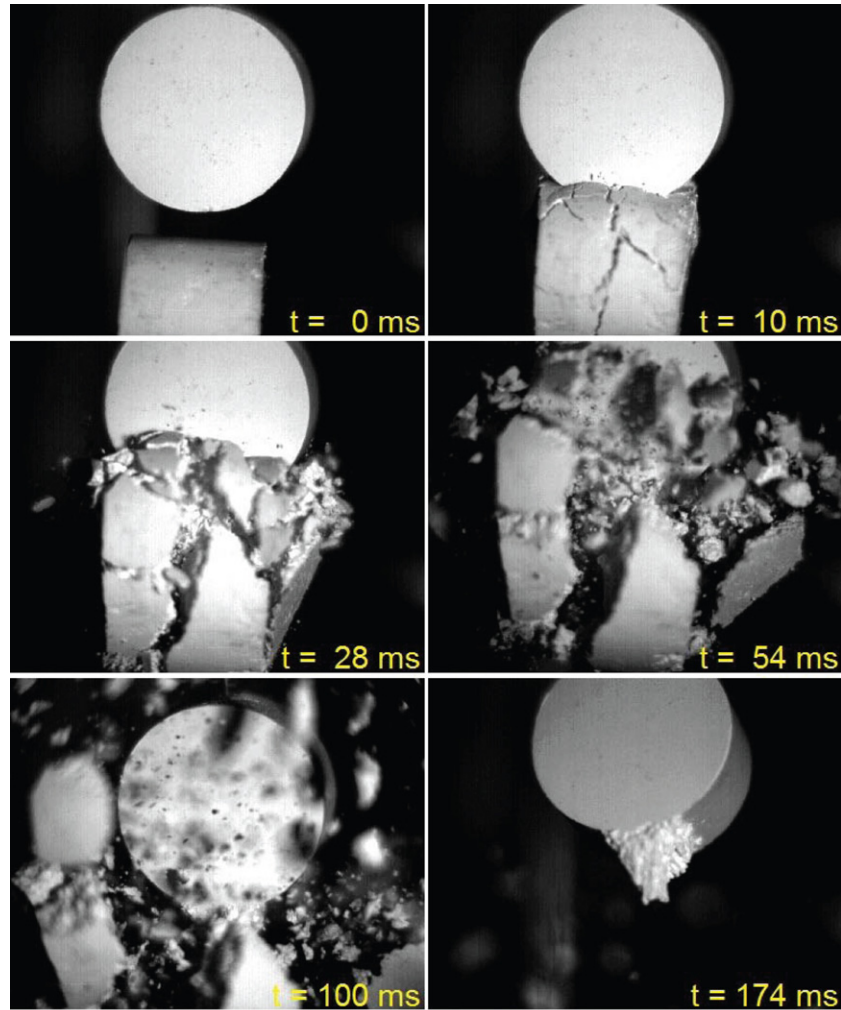
Figure 9. Image sequence that illustrates a collision between the cylindrical samples. Here, the collision velocity is roughly 1 m s^{-1}.
(An animation and a color version of this figure are available in the online journal.)

that it can be described by the linear relation

$$\mu^{+}(v) = \left(-4.3 \times 10^{-4} + 6.0 \times 10^{-3} \cdot \left(\frac{v}{\mathrm{m\,s^{-1}}} \right) \right) + 1. \quad (6)$$

More details on the accretion efficiency are given in the next section.

3.3. Accretion Efficiency

To further study the accretion efficiency as a function of the porosity difference and collision velocity, we first kept the porosity difference constant at 0.091 ± 0.014 for 20 experiments and varied the collision velocity from 0.5 to 1.4 m s^{-1}. We used the setup shown in Figure 3 for this. In the second step, we performed 24 experiments at a constant collision velocity of (0.93 ± 0.08) m s^{-1} and varied the porosity difference between the aggregates from 0.03–0.13. The target aggregate—the upper aggregate, which was more compact and thus robust—always gained mass, as seen in Figure 9. After capturing the intact aggregate, we were able to measure the accretion efficiency e_{ac}, i.e., the mass growth in units of the projectile mass. For a few examples, the mass growth was also deduced from the images using the same approach as that presented for the drop-tower experiments. Here, the deduction of mass growth from the images is in good agreement with the measured accretion

efficiency. For this reason, it can be concluded that the volume-filling factor of the cone remains unchanged compared with the projectile-filling factor.

The mass gain's dependence on the collision velocity is presented in Figure 10; the gray circles represent single experiments. Below 0.5 m s^{-1}, no mass growth and only bouncing collisions without mass transfer were observed (two data points at $e_{ac} = 0$). Therefore, we can confirm a low-velocity cutoff, where collisions are not energetic enough for sufficient inelastic interaction, i.e., to lead to fragmentation. The values above 0.5 m s^{-1} are averaged in steps of 0.2 m s^{-1} up to 1.5 m s^{-1}, which are shown by the black squares. An increase in mass gain with collision velocity is clearly visible: faster collisions lead to a higher mass gain. We assumed a linear increase and fitted a straight line,

$$e_{ac}(v, \Delta\phi = 0.091) = -3.5 \times 10^{-3} + 2.5 \times 10^{-2} \left(\frac{v}{\mathrm{m\,s^{-1}}} \right), \quad (7)$$

to the raw data (neglecting the first point at $e_{ac} = 0$). The black triangles are the results from the experiments in the drop-tower setup presented in the previous section and show a similar trend. The lower values can be explained by a smaller difference in porosity (see below and Section 4).

The mass gain as a function of the measured porosity difference of colliding aggregates is shown in Figure 11;
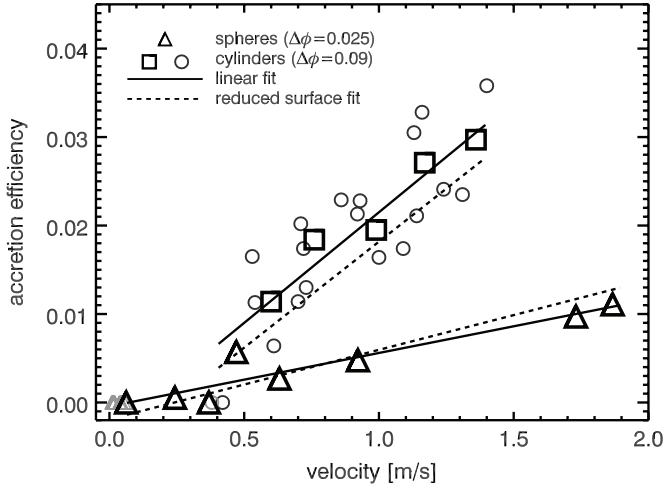
Figure 10. Mass gain over collision velocity at constant porosity difference $\Delta\phi = 0.091$. Each gray circle represents one experiment, the black line is a linear fit to these data points, and black squares are averaged values to illustrate the linear trend. Results from the drop tower are presented as triangles and are also linearly fitted (lower solid line). The dotted lines are the results of the two-dimensional fit, which is discussed in Section 4.
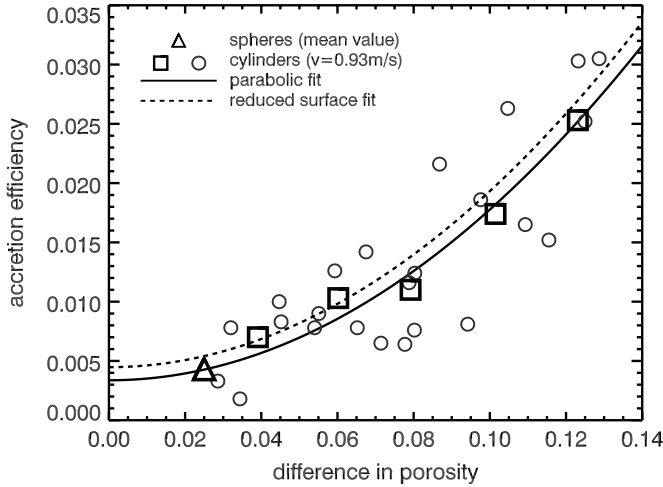

Figure 11. Mass gain as a function of porosity difference for a constant collision velocity of 0.93 m s^{-1}. The gray circles show the raw data, the solid curve is a fit to these data according to Equations (8) and (9) (these equations are indistinguishable from each other in the parameter range shown), and the black squares represent averaged values. The triangle shows the mean accretion efficiency of all drop-tower experiments. The dashed curve is discussed in Section 4.

again, the gray circles denote individual experiments. A trend of increasing accretion efficiency with increasing porosity difference is already visible in the raw data and becomes even clearer after averaging steps of 0.02 in porosity. Without further justification but to give a simple mathematical expression, we fitted a parabolic curve to the raw data, given as

$$e_{ac,par}(\Delta\phi, v = 0.93 \text{ m s}^{-1}) = 3.4 \times 10^{-3} + 1.44 \cdot \Delta\phi^2 \quad (8)$$

which is shown as a solid line in Figure 11. Alternatively, an exponential function given as

$$e_{ac,exp}(\Delta\phi, v = 0.93 \text{ m s}^{-1}) = 4.4 \times 10^{-3}$$
$$+ 1.2 \times 10^{-3} \cdot \exp(23 \cdot \Delta\phi) \quad (9)$$

can hardly be distinguished from the previous curve and gives a similar (even slightly better) reduced χ^2. Both curves fit
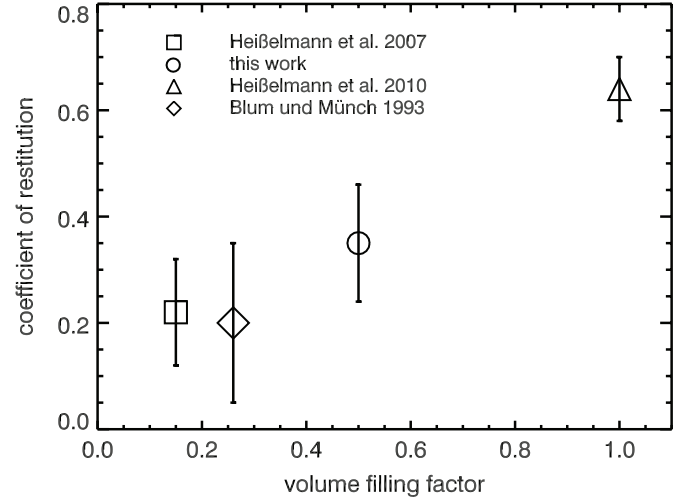

Figure 12. Coefficient of restitution of various experiments as a function of the volume-filling factor. Although very clear, this trend should only be regarded as qualitative because of the difference in samples, impact parameter, and collision velocity.

the data in the presented range but significantly deviate with higher porosity differences: the exponential function gives an accretion efficiency of 0.5 for a porosity difference of 0.26, while for the parabolic function this happens at a porosity difference of 0.59. An extrapolation of this curve is dangerous and not recommended, but the consequences would be that the parabolic function predicts a limited mass transfer, even for the highest possible porosity differences, while the exponential function predicts a saturation or the onset of a new effect for porosity differences as small as 0.3. This can be tested in future experiments.

4. DISCUSSION

Depending on collision velocity, we qualitatively found three different collisional outcomes that comprise bouncing, fragmentation with mass transfer, and complete fragmentation. In Figure 8, we presented a conclusive overview of the outcomes in the drop-tower experiments that gives us the velocity range of these effects:

$v < 40 \text{ cm s}^{-1}$: bouncing
$v > 20 \text{ cm s}^{-1}$: partial fragmentation
$v < 190 \text{ cm s}^{-1}$: with mass transfer
$v > 190 \text{ cm s}^{-1}$: disruptive fragmentation.

Bouncing collisions were presented in Section 3.1, and the main result was a mean coefficient of restitution of 0.35 ± 0.12, where the error does not represent the measurement precision but the standard deviation resulting from the natural scatter of the data. To compare these results with earlier experiments, we present the coefficient of restitution as a function of the volume-filling factor for various experiments (Figure 12). These experiments are all different: while Heißelmann et al. (2007) used the same dust material as we did in our drop-tower experiments and a similar velocity (20 cm s^{-1}), the aggregates had a cubic shape and the volume-filling factor was much lower ($\phi = 0.15$). Blum & Münch (1993) performed near-central collisions between aggregates of ZrSiO$_4$ dust with a comparable grain size and a volume-filling factor of $\phi = 0.26$. The fourth data point is from Heißelmann et al. (2010), who used solid
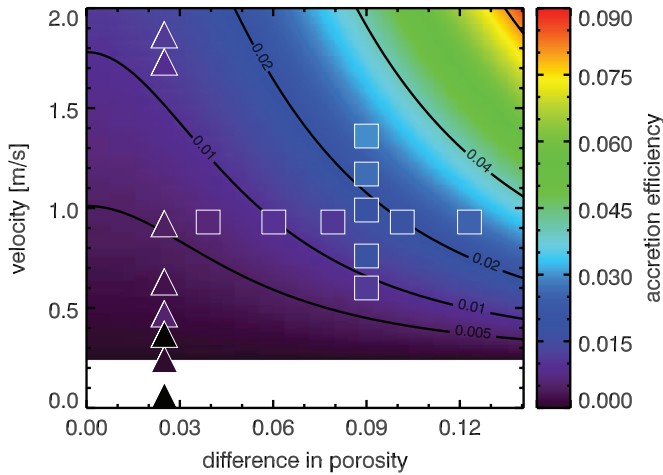
Figure 13. Two-dimensional fit interpolating the mass accretion as a function of velocity and porosity difference according to Equation (10). The data points represent the measured accretion efficiency in color; for the experiment with cylinders, we only show the mean values.

(A color version of this figure is available in the online journal.)

Figure 14. Fragmentation strength as a function of impact velocity. The triangles, squares, and circles show the data from Figure 8, Blum & Münch (1993), and Lammel (2008), respectively. The dashed and solid lines are power-law fits to these data (see Equation (11)).

(A color version of this figure is available in the online journal.)

glass beads (still SiO_2), with all possible impact parameters in a multiple-collision experiment within a range of velocities $(0.3–5 \text{ cm s}^{-1})$. In spite of these differences, a clear trend is obvious: porous aggregates behave more inelastically and thus dissipate more energy than compact aggregates or solid samples. This trend is much stronger than the dependence on the collision velocity, which we could not resolve in Section 3.1.

For velocities around 20 cm s^{-1}, we found that particle fragmentation sets in, which means that only one aggregate is destroyed and transfers mass to the other particle. In Figures 10 and 11, we presented the accretion efficiency as a function of collision velocity and porosity difference. From these, we now want to give a full equation for $e_{ac}(v, \Delta\phi)$. We cannot simply multiply Equations (7) and (8) (or Equation (9), respectively) because these do not exactly match at $v = 0.93 \text{ m s}^{-1}$ and $\Delta\phi = 0.091$. We therefore fitted the raw data points from the experiments with the cylindrical samples using the function

$$e_{ac}(v, \Delta\phi) = \left(a + b \cdot \Delta\phi^2\right) \cdot (c + d \cdot v). \qquad (10)$$

A special search technique similar to the downhill simplex algorithm was used to obtain the parameters. The calculated parameters are $a = 0.26$, $b = 85$, $c = -6.1 \times 10^{-3}$, and $d = 2.5 \times 10^{-2} \text{ s m}^{-1}$. Equation (10) can again be reduced to the constant porosity difference and constant velocity for which the series of experiments were conducted, which are presented in Figures 10 and 11 as the dashed line. Those are still in the range of the errors and differ only slightly from the original functions. The combination of both parameters is presented in the contour plot of Figure 13. The color values correspond to Equation (10), and the color of the squares represents the value of the averaged data (Figures 10 and 11). The white region at low velocities ($v \lesssim 25 \text{ cm s}^{-1}$) is where Equation (10) mathematically predicts a negative mass transfer, but we expect bouncing collisions. This is supported by the black triangles, representing bouncing collisions without mass transfer. Due to the difference in aggregate geometry and grain shape, the results from the drop-tower experiments were not utilized to compute the fit in Equation (10), but they are nonetheless very well represented by this curve (see triangles in Figure 13). If we reduce the equation again to the constant
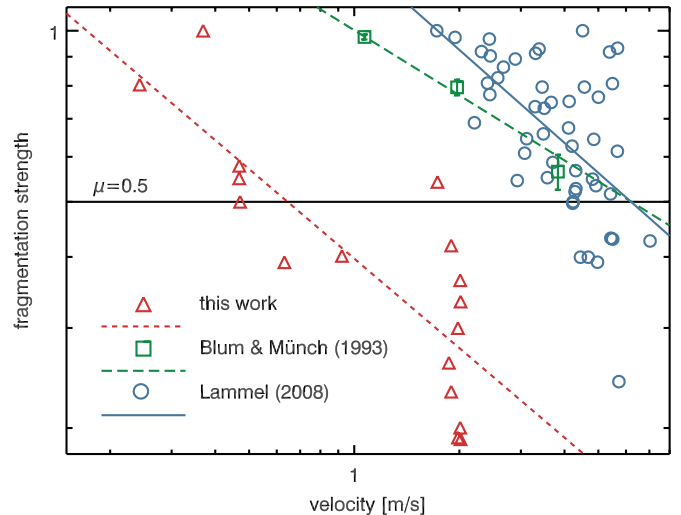
porosity difference $\Delta\phi = 0.025$, we find in Figure 10 that the dashed line is very close to the solid line. This agreement, without further assumptions, ensures that the experiments are highly comparable in spite of the discussed differences. We therefore regard Equation (10) as a good description of the mass transfer in a disruptive collision between two aggregates with different strengths. The validity range of this equation is given by $20 \text{ cm s}^{-1} < v < 190 \text{ cm s}^{-1}$ in velocity. For porosity, we cannot make a definite prediction for $\Delta\phi > 0.13$, which is the maximum value that was studied here.

The velocity of 20 cm s^{-1}, where fragmentation sets in, is significantly lower than expected from experiments with millimeter-sized aggregates (Güttler et al. 2010). We therefore expect that the threshold velocity is size-dependent and compare our results with the data of Blum & Münch (1993) and Lammel (2008), who measured the strength of fragmentation for variable velocities, as presented here in Section 3.2. We consider central collisions and take the mean values from Figure 7 in Blum & Münch (1993), as well as raw data from Lammel (2008). These are presented in Figure 14, where the red triangles represent our data from Section 3.2, the green squares represent the values of Blum & Münch (1993; mean values, thus including errors), and the blue circles represent the data of Lammel (2008). From these, we get equations similar to Equation (5), which relates the fragmentation strength to the collision velocity between two dust aggregates. In its general form, this reads as

$$\mu = \left(\frac{v}{v_0}\right)^{-\alpha}. \qquad (11)$$

Our data, presented in Figure 8, yield $v_0 = (0.17^{+0.07}_{-0.05}) \text{ m s}^{-1}$ and $\alpha = 0.52 \pm 0.10$ for collisions between equal-sized dust aggregates with masses of $m = 4.1 \text{ g}$ and radii of $s = 1 \text{ cm}$ (short, dashed red line in Figure 14). For collisions between millimeter-sized dust aggregates, i.e., for the data of Blum & Münch (1993) (using aggregates with $m = 4 \text{ mg}$ and $s = 0.9 \text{ mm}$ consisting of micrometer-sized $ZrSiO_4$), we get $v_0 = (1.01 \pm 0.03) \text{ m s}^{-1}$ and $\alpha = 0.38 \pm 0.04$ (long, dashed green line). For the data of Lammel (2008) (using aggregates with $m = 1 \text{ mg}$ and $s = 0.7 \text{ mm}$ consisting of μm-sized SiO_2; s is the

half-edge length of the cubic aggregates here), the parameters are $v_0 = (1.73^{+0.63}_{-0.46})$ m s^{-1} and $\alpha = 0.54 \pm 0.11$ (solid blue line). These relations between fragmentation strength and velocity can be used to derive the velocity of the onset of fragmentation, i.e., $v_{1.0} = v(\mu = 1.0) = v_0$, and of the case when the largest fragment possesses half the mass of the original projectile aggregate, i.e., $v_{0.5} = v(\mu = 0.5) = v_0 \cdot 0.5^{-1/\alpha}$. Applying this to all data in Figure 14, we get $v_{0.5} = 0.64$ m s^{-1} for our data and $v_{0.5} = 6.2$ m s^{-1} for the data of Blum & Münch (1993) as well as for those of Lammel (2008); the velocity of the onset of fragmentation is already given by the fit parameter v_0. These velocities can be converted into specific energies, assuming equal-mass collision partners, by the relation $Q_x = \frac{1}{4} v_x^2$, with $x = 1.0$ or $x = 0.5$. We want to claim a relation between the critical fragmentation energy and aggregate size, but we have to be careful when comparing these data because the volume-filling factors significantly differ, from 0.15 (Lammel 2008) to 0.5 (our work).

The porosity has an effect on the strength of the aggregates as well as on the transmission of impact stress waves. The tensile strength of these aggregates is given by

$$T(\phi) = -(10^{2.8 + 1.48 \cdot \phi}) \tag{12}$$

(Güttler et al. 2009; their Equation (8)). For the relation between aggregate strength and fragmentation energy, we consider the results of Setoh et al. (2010) and Machii & Nakamura (2011) and take $Q \propto T^{3/4}$. The effect of poor shock transmission in porous media was studied by Love et al. (1993), who found a porosity dependence of $Q \propto \phi^{-3.6}$ if the strength of the bodies remained constant with changing porosity. In their numerical simulation of the disruption of larger bodies, Jutzi et al. (2010) also found that porous targets are more difficult to disrupt. Thus, following Love et al. (1993), we apply the correction

$$Q_x(\phi = 0.5) = Q_x(\phi) \frac{0.5^{-3.6} 10^{1.11 \times 0.5}}{\phi^{-3.6} 10^{1.11 \cdot \phi}}, \tag{13}$$

where $Q_x(\phi)$ is the critical energy for the individual experiments as calculated above and $Q_x(\phi = 0.5)$ is the critical energy corrected to a volume-filling factor of $\phi = 0.5$, as used in our experiments. With this equation, we arrive at Figure 15, where the critical fragmentation energies $Q_{0.5}$ and $Q_{1.0}$ for the three experiments are presented as a function of aggregate size. A power-law fit to these data of the form

$$Q_x^* = \left(\frac{s}{s_x} \right)^{-\beta} \text{J kg}^{-1} \tag{14}$$

yields $\beta = 0.95 \pm 0.38$, $s_{0.5} = (1.0^{+0.3}_{-0.2}) \times 10^{-3}$ m, and $s_{1.0} = (3.4^{+2.8}_{-1.2}) \times 10^{-5}$ m. We note that the slope should be regarded as an estimate, and it is desirable to conduct another experiment to measure the fragmentation energy for different-sized samples using the same strength and porosity. Consequently further studies are currently being prepared.

Our slope is slightly steeper than that of the material-strength regime presented by Benz & Asphaug (1999; see Figure 15), who studied collisions between rocky bodies in computer simulations. Our firm absolute values for $Q_{0.5}^*$ are several orders of magnitude smaller than those experimentally measured by Setoh et al. (2007) and Ryan et al. (1991; see Figure 15), who used sintered glass beads and weakly glued gravel, respectively. Machii & Nakamura (2011) also performed experiments with
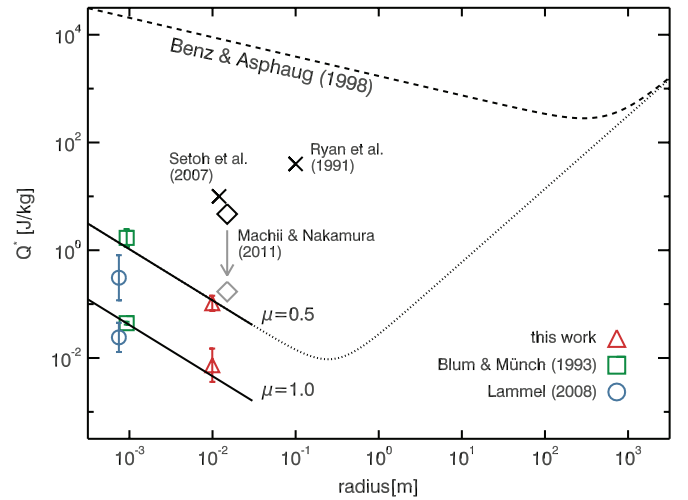

Figure 15. Critical fragmentation strength Q^* as a function of dust-aggregate radius for our data (triangles), as well as for the data of Blum & Münch (1993; squares) and Lammel (2008; circles). A least-squares power-law fit after Equation (14) is shown as a solid line for two cases: $\mu = 1.0$ and $\mu = 0.5$. Also shown are the Q^* data of Setoh et al. (2007) and Ryan et al. (1991; crosses), as well as the curve by Benz & Asphaug (1999; dashed line). The dotted line is an extrapolation of our data according to the model by Benz & Asphaug (1999).
(A color version of this figure is available in the online journal.)

sintered glass beads (black diamond in Figure 15) and found a dynamic strength on the same order of magnitude as Setoh et al. (2007) and Ryan et al. (1991). However, they also measured the static tensile strength of the material (3.5×10^5 Pa), and if we apply a similar scaling to the one above, we arrive at the gray diamond, which is in good agreement with our results. Although not perfectly applicable to our samples, we use the model by Benz & Asphaug (1999) for the strength of the gravitational regime. Actually, in a recent study by Jutzi et al. (2010), the slopes in the gravity regime (cf. their Table 3) are mostly comparable with those of Benz & Asphaug (1999), even if they use porous bodies, so we take

$$Q_{0.5}^* = \left\{ \left(\frac{s}{1 \text{ mm}} \right)^{-0.95} + \left(\frac{s}{15 \text{ m}} \right)^{1.36} \right\} \text{J kg}^{-1}, \tag{15}$$

illustrated by the dotted line in Figure 15. The first term is simply given by Equation (14), while the second term is taken from the gravity regime in Benz & Asphaug (1999; cf. their Equation (6) and Table 3, assuming a bulk density of 1000 kg m^{-3}. Thus, our measurements suggest that the weakest bodies in PPDs have radii of the order of 30 cm. Their strength should be around $Q^* = 10^{-2}$ J kg^{-1}, which corresponds to impact velocities between equal-sized particles of about 0.2 m s^{-1}. A comparison to the expected collision velocities in different PPD models (see Figure 8 in Weidling et al. 2009) shows that the collision velocities for decimeter-sized aggregates exceed this critical fragmentation velocity in both the MMSN model (Weidenschilling 1977) and the low-density model by Andrews & Williams (2007). The collision velocities in the high-density model by Desch (2007) are comparable to our estimated fragmentation velocity for decimeter-sized dust aggregates. Thus, dust aggregates of decimeter size can barely survive mutual collisions if the impact velocities are moderate. Alternatively, the strength of aggregates against fragmentation increases if the aggregates experience any solidification process, e.g., by sintering (see data by Setoh et al. 2007 and Ryan et al. 1991 in Figure 15).

REFERENCES

Andrews, S. M., & Williams, J. P. 2007, ApJ, 659, 705
Benz, W., & Asphaug, E. 1999, Icarus, 142, 5
Blum, J., & Münch, M. 1993, Icarus, 106, 151
Blum, J., & Schräpler, R. 2004, Phys. Rev. Lett., 93, 115503
Blum, J., & Wurm, G. 2008, ARA&A, 46, 21
Desch, S. J. 2007, ApJ, 671, 878
Güttler, C., Blum, J., Zsom, A., Ormel, C. W., & Dullemond, C. P. 2010, A&A, 513, A56
Güttler, C., Krause, M., Geretshauser, R. J., Speith, R., & Blum, J. 2009, ApJ, 701, 130
Heim, L.-O., Blum, J., Preuss, M., & Butt, H.-J. 1999, Phys. Rev. Lett., 83, 3328
Heißelmann, D., Blum, J., Fraser, H. J., & Wolling, K. 2010, Icarus, 206, 424
Heißelmann, D., Fraser, H., & Blum, J. 2007, in Proc. 58th International Astronautical Congress 2007 (Paris: International Astronautical Federation), IAC-07-A2.1.02, http://www.iafastro.net/iac/archive/browse/IAC-07/A2./1./6811/
Jutzi, M., Michel, P., Benz, W., & Richardson, D. C. 2010, Icarus, 207, 54
Lammel, C. 2008, Bachelor's thesis, Technische Universität Carolo Wilhelmina zu Braunschweig
Love, S. G., Hörz, F., & Brownlee, D. E. 1993, Icarus, 105, 216
Machii, N., & Nakamura, A. M. 2011, Icarus, 211, 885
Ryan, E. V., Hartmann, W. K., & Davis, D. R. 1991, Icarus, 94, 283
Setoh, M., Hiraoka, K., Nakamura, A. M., Hirata, N., & Arakawa, M. 2007, Adv. Space Res., 40, 252
Setoh, M., Nakamura, A. M., Michel, P., Hiraoka, K., Yamashita, Y., Hasegawa, S., Onose, N., & Okudaira, K. 2010, Icarus, 205, 702
Weidenschilling, S. J. 1977, Ap&SS, 51, 153
Weidenschilling, S. J., & Cuzzi, J. N. 1993, in Protostars and Planets III, ed. E. H. Levy & J. I. Lunine (Tucson, AZ: Univ. Arizona Press), 1031
Weidling, R., Güttler, C., Blum, J., & Brauer, F. 2009, ApJ, 696, 2036
Zsom, A., Ormel, C. W., Güttler, C., Blum, J., & Dullemond, C. P. 2010, A&A, 513, A57